CHIN. PHYS. LETT. Vol. 38, No. 8 (2021) 084501

Chiral Anomaly-Enhanced Casimir Interaction between Weyl Semimetals

Jia-Nan Rong(荣佳楠)[1,3], Liang Chen(陈亮)[2*], and Kai Chang(常凯)[1,3*]

[1]*SKLSM, Institute of Semiconductors, Chinese Academy of Sciences, Beijing 100083, China*
[2]*School of Mathematics and Physics, North China Electric Power University, Beijing 102206, China*
[3]*CAS Center for Excellence in Topological Quantum Computation, University of Chinese Academy of Sciences, Beijing 100190, China*

(Received 16 May 2021; accepted 22 June 2021; published online 2 August 2021)

We theoretically study the Casimir interaction between Weyl semimetals. When the distance a between semi-infinite Weyl semimetals is in the micrometer regime, the Casimir attraction can be enhanced by the chiral anomaly. The Casimir attraction depends sensitively on the relative orientations between the separations ($\boldsymbol{b}_1$, $\boldsymbol{b}_2$) of Weyl nodes in the Brillouin zone and show anisotropic behavior for the relative orientation of these separations ($\boldsymbol{b}_1$, $\boldsymbol{b}_2$) when they orient parallel to the interface. This anisotropy is quite larger than that in conventional birefringent materials. The Casimir force can be repulsive in the micrometer regime if the Weyl semimetal slabs are sufficiently thin and the direction of Weyl nodes separations ($\boldsymbol{b}_1$, $\boldsymbol{b}_2$) is perpendicular to the interface. The Casimir attraction between Weyl semimetal slabs decays slower than $1/a^4$ when the Weyl nodes separations $\boldsymbol{b}_1$ and $\boldsymbol{b}_2$ are both parallel to the interface.

DOI: 10.1088/0256-307X/38/8/084501

The quantum fluctuation of electromagnetic (EM) field can induce an attractive force between two parallel, perfect conducting, uncharged slabs. This phenomenon is known as the Casimir effect.[1] In 1955, Lifshitz developed a general framework to describe the Casimir and van der Waals interactions. For spatial dimensions from a few micrometers to nanometers, the Casimir–Lifshitz interaction plays an important role, which dominates the fabrication, performance and function of micro- and nano-electromechanical systems. Casimir physics is an attractive topic for both theoretical and experimental studies in the past decades. Exotic proposals in this field have been verified in the past few years, e.g., the repulsive Casimir interaction[2] between dielectrics with the liquid filled in between, thermal Casimir effect[3] (the thermal fluctuation of virtual photons), critical Casimir effect induced by thermal fluctuation near the phase transition point,[4] dynamical Casimir effect,[5] Casimir–Lifshitz torque between liquid crystal and birefringent material,[6] etc.

Casimir repulsion has attracted great attention for the quantum levitation and significant reduction of friction in micromechanical systems. Casimir repulsions have been investigated in different systems, e.g., by using special geometry[7] or chiral metamaterial,[8] applying adjustable magnetic field,[9] filling high-reflective liquid between dielectrics,[2] inserting left-handed metamaterial[10] or optical active materials[11] between plates, and utilizing the rotation of the particle near a bi-isotropic material.[12] In recent years, Casimir repulsions between topological materials, i.e., topological insulators,[13] quantum Hall slabs,[14] Chern insulators,[15] and Weyl semimetals (WSMs),[16] have been widely studied. The (anomalous) Hall conductivity induced non-vanishing off-diagonal elements of the Fresnel matrix are crucial for the formation of Casimir repulsion in topological materials.

Weyl semimetal[17] provides a new platform for the investigation of Weyl fermions.[18,19] A pair of Weyl nodes with opposite chiralities in the Brillouin zone have the same nature as massless Weyl fermions in quantum field theory.[20–22] Chiral anomaly[23,24] is the unique nature of Weyl fermions. Significant evidence of chiral anomalies for the recent discovered WSMs have been reported, e.g., the surface fermi arc, chiral magnetic effect and negative longitudinal magnetoresistance.[25,26] The topological nontrivial EM response of WSM provides another approach for the identification of chiral anomaly.[27–31] In quantum field theory, the universal part of the chiral anomaly is described by the θ term in the action, $\mathcal{S}_\Theta = \frac{e^2}{32\pi^2}\int dtd^3r[\Theta(t,\boldsymbol{r})\varepsilon^{\mu\nu\rho\sigma}F_{\mu\nu}F_{\rho\sigma}]$. Here $\Theta(t,\boldsymbol{r}) = -2b_0t + 2\boldsymbol{b}\cdot\boldsymbol{r}$, $(2b_0, 2\boldsymbol{b})$ is the separation of the two Weyl nodes in the energy and momentum spaces. In this work, we give a systematic investigation of the Casimir interactions between WSM slabs. All possible configurations are considered: the separations of Weyl nodes, $\boldsymbol{b}_1$ and $\boldsymbol{b}_2$, are both perpendicular to or parallel to the interfaces for finite and semi-infinite WSMs cases. We focus on the chiral anomaly induced variations in Casimir physics, especially when the distance, a, is in the micrometer regime. Detailed

Supported by the Strategic Priority Research Program of Chinese Academy of Sciences (Grant No. XDB28000000), the National Natural Science Foundation of China (Grant Nos. 61674145, 11974340, and 11504106), the National Key R&D Program of China (Grant Nos. 2017YFA0303400 and 2018YFA0306101), the Chinese Academy of Sciences (Grant No. QYZDJ-SSW-SYS001 and XDPB22).
*Corresponding authors. Email: slchern@ncepu.edu.cn; kchang@semi.ac.cn

illustration of Casimir interaction between WSM slabs is given in Fig. 1.

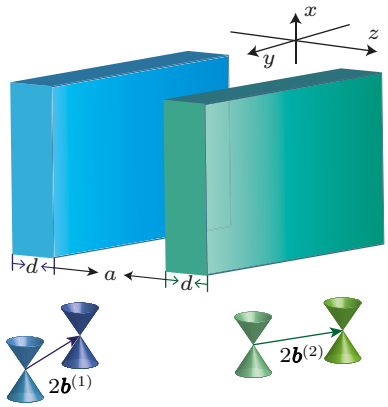

Fig. 1. Illustration of Casimir interaction between WSM slabs. Upper panel: two WSM slabs with thickness d are separated in the vacuum with distance a. The interfaces of WSMs and the vacuum are chosen to be perpendicular to the z-axis. Lower panel: The separation of Weyl nodes in the Brillouin zone for the two WSM slabs, $2\boldsymbol{b}^{(1)}$, $2\boldsymbol{b}^{(2)}$. When $2\boldsymbol{b}^{(1)}$ and $2\boldsymbol{b}^{(2)}$ are parallel to the interface, θ_1 and θ_2 are used to describe the angles between these vectors and the x-axis. Here $\theta_2 - \theta_1$ describes the twisting angle of the two WSMs.

According to the effective action, we can obtain the EM response of WSMs with chiral anomaly correction,[28,31,32] i.e., the modified Maxwell equations,

$$\nabla \cdot \boldsymbol{D} = \eta \boldsymbol{e}^{(j)} \cdot \boldsymbol{B}, \tag{1}$$

$$\nabla \times \boldsymbol{H} = \frac{1}{c}\frac{\partial \boldsymbol{D}}{\partial t} - \eta \boldsymbol{e}^{(j)} \times \boldsymbol{E}, \tag{2}$$

$$\nabla \cdot \boldsymbol{B} = 0, \tag{3}$$

$$\nabla \times \boldsymbol{E} = -\frac{1}{c}\frac{\partial \boldsymbol{B}}{\partial t}, \tag{4}$$

where $\eta = 2e^2 b/\pi\hbar c$ describes the strength of chiral anomaly in WSM, $\boldsymbol{e}^{(j)}$ is the unit vector parallel to the separation of the two Weyl nodes in the Brillouin zone for the j-th WSM ($j = 1, 2$). $\boldsymbol{D} = \varepsilon \boldsymbol{E}$, $\boldsymbol{H} = \boldsymbol{B}/\mu$, with ε and μ being the permittivity and permeability.

The zero-temperature Casimir energy density stored in between two WSM slabs can be calculated using the Casimir–Lifshitz formula,

$$\frac{E_C(a)}{A} = \frac{\hbar}{8\pi^3}\int_0^\infty d\zeta \int d\boldsymbol{k}_\parallel \cdot \ln\det\left[\mathbb{I} - e^{-2\kappa a}\mathbb{R}^{(1)}(i\zeta, \boldsymbol{k}_\parallel)\cdot\mathbb{R}^{(2)}(i\zeta, \boldsymbol{k}_\parallel)\right], \tag{5}$$

where A is the surface area of the WSM slabs, $\mathbb{I}$ is the 2×2 identity matrix, ζ is the imaginary frequency, $\boldsymbol{k}_\parallel = (k_x, k_y)$ is the wave vector parallel to the interface, $\kappa = \sqrt{\boldsymbol{k}_\parallel^2 + \zeta^2/c^2}$, $\mathbb{R}^{(1)}(i\zeta, \boldsymbol{k}_\parallel)$ and $\mathbb{R}^{(2)}(i\zeta, \boldsymbol{k}_\parallel)$ are the Fresnel matrices of the two inside interfaces. The Casimir force density is defined as

$$\frac{F_C(a)}{A} = -\frac{1}{A}\frac{\partial E_C(a)}{\partial a}. \tag{6}$$

The Fresnel matrices in Eq. (5) can be solved using the Berreman matrix method.[33] We can find the following universal expressions of the reflection matrices (see the Supplementary Materials for Berreman matrices, detailed derivation and analytical expressions of the reflection matrices):

$$\mathbb{R}^{(1)}_{\rm Cart} = [k_3\mathbb{T}^{(1)}_{11} - \mathbb{T}^{(1)}_{12}\mathbb{Q}][k_3\mathbb{T}^{(1)}_{21} - \mathbb{T}^{(1)}_{22}\mathbb{Q}]^{-1}, \tag{7}$$

$$\mathbb{R}^{(2)}_{\rm Cart} = [k_3\mathbb{T}^{(2)}_{21} + \mathbb{T}^{(2)}_{22}\mathbb{Q}][k_3\mathbb{T}^{(2)}_{11} + \mathbb{T}^{(2)}_{12}\mathbb{Q}]^{-1}, \tag{8}$$

where the subindex *Cart* denotes that the reflection matrices are calculated in the Cartesian coordinates, $k_3 = \sqrt{\boldsymbol{k}_\parallel^2 - \omega^2/c^2}$ and ω is the frequency of EM waves, $\mathbb{Q}$ is a 2×2 matrix that describes the propagation of EM waves in vacuum. The 4×4 matrix

$$\mathbb{T}^{(j)} = \begin{pmatrix} \mathbb{T}^{(j)}_{11} & \mathbb{T}^{(j)}_{12} \\ \mathbb{T}^{(j)}_{21} & \mathbb{T}^{(j)}_{22} \end{pmatrix}$$

is the transfer matrix of the j-th WSM slab. The explicit expressions of these transfer matrices are

$$\mathbb{T}^{(1)} = [\mathbb{W}]^{-1}[\mathbb{W}^{(1)}]e^{-\mathbb{K}^{(1)}d}[\mathbb{W}^{(1)}]^{-1}, \tag{9}$$

$$\mathbb{T}^{(2)} = [\mathbb{W}]^{-1}[\mathbb{W}^{(2)}]e^{+\mathbb{K}^{(2)}d}[\mathbb{W}^{(2)}]^{-1}, \tag{10}$$

where $\mathbb{W}$, $\mathbb{W}^{(1)}$ and $\mathbb{W}^{(2)}$ in Eqs. (9) and (10) consist of the four eigen vectors of the Berreman matrices in the vacuum and the two WSM slabs, respectively. $\mathbb{K}^{(1)}$ and $\mathbb{K}^{(2)}$ are the corresponding eigenvalues of the Berreman matrices in the WSM slabs. Table 1 shows detailed expressions of $\mathbb{K}^{(j)}$ for different configurations.

Table 1. Matrix $\mathbb{K}^{(j)} = \mathrm{diag}[\lambda_1^{(j)}, \lambda_2^{(j)}, -\lambda_2^{(j)}, -\lambda_1^{(j)}]$ for different configurations. In the following expressions, $p_3 = \sqrt{\boldsymbol{k}_\parallel^2 - \varepsilon\omega^2/c^2}$, $\delta^{(j)} = \sqrt{\eta^2 + 4\varepsilon[\boldsymbol{k}_\parallel \cdot \boldsymbol{e}^{(j)}]^2}$.

$\boldsymbol{b}^{(j)} \parallel \boldsymbol{e}_z$	$\lambda_1^{(j)} = \sqrt{p_3(p_3 - i\eta/\sqrt{\varepsilon})}$, $\lambda_2^{(j)} = \sqrt{p_3(p_3 + i\eta/\sqrt{\varepsilon})}$
$\boldsymbol{b}^{(j)} \perp \boldsymbol{e}_z$	$\lambda_1^{(j)} = \sqrt{p_3^2 + \eta[\eta + \delta^{(j)}]/2\varepsilon}$, $\lambda_2^{(j)} = \sqrt{p_3^2 + \eta[\eta - \delta^{(j)}]/2\varepsilon}$

Thus far, we obtain the complete calculation formula of reflection matrices $\mathbb{R}^{(1)}_{\rm Cart}$ and $\mathbb{R}^{(2)}_{\rm Cart}$. For the practical evaluation of Casimir force, three issues should be clarified. Firstly, in the Casimir–Lifshitz formula, Eq. (5), the Fresnel matrices $\mathbb{R}^{(1)}$ and $\mathbb{R}^{(2)}$ are decomposed into the transverse electric and transverse magnetic modes. $\mathbb{R}^{(1)}_{\rm Cart}$ and $\mathbb{R}^{(2)}_{\rm Cart}$ shown in Eqs. (7) and (8) are expressed in the Cartesian coordinates. After some straightforward derivation, we find that $\mathbb{R}^{(1)}$, $\mathbb{R}^{(2)}$ and $\mathbb{R}^{(1)}_{\rm Cart}$, $\mathbb{R}^{(2)}_{\rm Cart}$ are related to each other via the following transformation,

$$\mathbb{R}^{(1)} = \begin{pmatrix} -\frac{k_y}{k_\parallel} & \frac{k_x}{k_\parallel} \\ \frac{kk_x}{k_\parallel k_z} & \frac{kk_y}{k_\parallel k_z} \end{pmatrix} \mathbb{R}^{(1)}_{\rm Cart} \begin{pmatrix} -\frac{k_y}{k_\parallel} & -\frac{k_x k_z}{k_\parallel k} \\ \frac{k_x}{k_\parallel} & -\frac{k_y k_z}{k_\parallel k} \end{pmatrix},$$

$$\mathbb{R}^{(2)} = \begin{pmatrix} -\frac{k_y}{k_\parallel} & \frac{k_x}{k_\parallel} \\ -\frac{kk_x}{k_\parallel k_z} & -\frac{kk_y}{k_\parallel k_z} \end{pmatrix} \mathbb{R}^{(2)}_{\rm Cart} \begin{pmatrix} -\frac{k_y}{k_\parallel} & \frac{k_x k_z}{k_\parallel k} \\ \frac{k_x}{k_\parallel} & \frac{k_y k_z}{k_\parallel k} \end{pmatrix}.$$

Here $k_\parallel = \sqrt{k_x^2 + k_y^2}$, $k = \sqrt{k_\parallel^2 + k_z^2}$. It is easy to check that the transformation of the multiplication $\mathbb{R}^{(1)}_{\rm Cart} \cdot \mathbb{R}^{(2)}_{\rm Cart} \to \mathbb{R}^{(1)} \cdot \mathbb{R}^{(2)}$ is unitary. Hence, we can safely replace $\mathbb{R}^{(1)} \cdot \mathbb{R}^{(2)}$ by $\mathbb{R}^{(1)}_{\rm Cart} \cdot \mathbb{R}^{(2)}_{\rm Cart}$ in the Casimir–Lifshitz formula. Secondly, the reflection matrices $\mathbb{R}^{(1)}_{\rm Cart}(\omega, \boldsymbol{k}_\parallel)$ and $\mathbb{R}^{(2)}_{\rm Cart}(\omega, \boldsymbol{k}_\parallel)$ are given in real-frequency representation. The analytical continuation, $\omega \to i\zeta$, is necessary in the evaluation of the Casimir–Lifshitz energy. Thirdly, for realistic WSM materials, the quantum fluctuation of virtual photon are effected by not only the proper boundary conditions and the optical conductivity of Weyl fermions near the Weyl nodes, but also the optical conductivity contributed from other energy bands in the bulk of WSMs, we describe these topological trivial contributions using the following Ninham–Parsegian oscillator model,

$$\varepsilon(i\zeta) = 1 + \sum_{j=1}^{K} \frac{g_j}{\omega_j^2 + \zeta^2 + \gamma_j \zeta}, \tag{11}$$

where ω_j and g_j are the oscillator frequency and oscillation strength of the j-th optical oscillator, γ_j is the damping parameter, K is the total number of oscillators. For realistic material TaAs,[18] we fit the parameters using the first-principle calculation.[34] The fitting parameters are given in Table 2 (the small damping parameters γ_j are chosen to be zero).

Table 2. Fitting parameters of the Ninham–Parsegian oscillator model given in Eq. (11).

j	1	2	3
$\hbar\omega_j$ (eV)	0.4066	1.1833	3.0650
g_j (eV^2)	0.3518	9.7594	26.1002

Figure 2 shows the Casimir force between two semi-infinite WSMs as a function of distance for different orientations of the Weyl node separations. The black line describes the Casimir force between normal dielectrics without chiral anomalies. In the large distance regime $a > 1\,\mu$m, the numerical calculation coincides with the analytical result,[35] $F(a) = -\chi_\infty \hbar c/32\pi^2 a^4$, where χ_∞ is an integration which depends only on the electrostatic dielectric constant $\varepsilon(0)$. For the parameters listed in Table 2, $\varepsilon(0) \approx 13$ gives $\chi_\infty = 4.09$ and $F(a)/F_0(a) = 0.315$. In the short distance limit, $a \to 0$, the numerical result is consistent with the asymptotic expression $F(a) = -\chi_0 \hbar/16\pi^2 a^3$,[34] where χ_0 is an integration that depends on the permittivity function $\varepsilon(i\zeta)$. For the parameters given in Table 2, $\chi_0 \approx 4.95$, which gives $F(a)/F_0(a) = 3.86 \times 10^{-3} a$ in SI units (see the dashed lines in Fig. 2 for the asymptotic behaviors). Clearly, one can see that the Casimir force can be enhanced by the chiral anomaly in the large distance regime, $a > 1\,\mu$m. In general, this can be understood from the eigenvalues of the Berreman matrices shown in Table 1. These eigenvalues determine the penetration length of the virtual photon in WSMs. At the large distance limit, $a \to \infty$, the Casimir force is dominated by the virtual photon with $\kappa \to 0$, so that $p_3 \to 0$. The chiral anomaly terms in the eigenvalues listed in Table 1 give significant corrections, which make the eigenvalues conspicuously larger than conventional dielectrics.

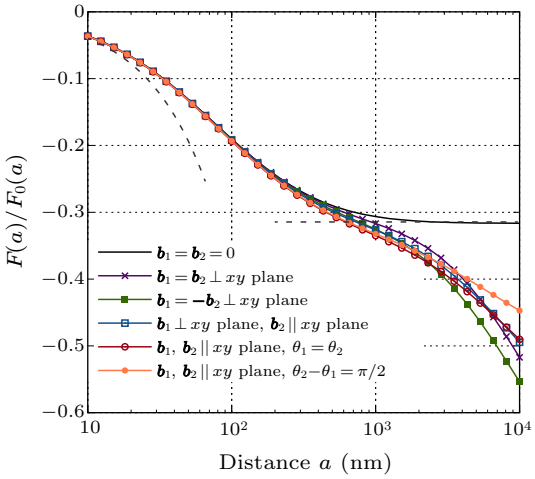

Fig. 2. Casimir force between two semi-infinite WSM slabs for different configures of the Weyl node separations, $\boldsymbol{b}_1$ and $\boldsymbol{b}_2$. $F_0(a) = \hbar c\pi^2/240a^4$ is the absolute value of Casimir force between ideal conductors. The dashed lines show the asymptotic behaviors of the black line ($\boldsymbol{b}_1 = \boldsymbol{b}_2 = 0$) for the small and large distances, respectively; $|\boldsymbol{b}_1| = |\boldsymbol{b}_2| = 0.08\,\text{Å}^{-1}$ for TaAs is fitted from experiment.[18]

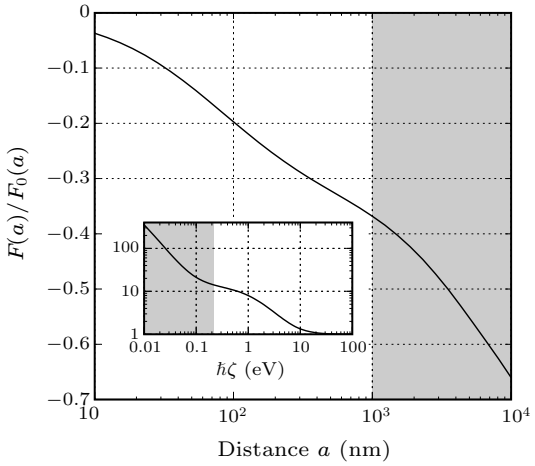

Fig. 3. Casimir force as a function of distance for $\boldsymbol{b}_1 = \boldsymbol{b}_2 = 0$ and an additional strong Drude term in the Ninham–Parsegian oscillator model. The insert shows the permittivity as a function of imaginary frequency when the Drude term is contained. In the far infrared regime, the Drude term induces a divergence of the permittivity.

We must point out that there is another important but completely different mechanism which can also enhance the Casimir attraction in the micrometer regime. The optical conductivity of the gapless quasiparticles in WSMs becomes divergent in the far infrared regime, which can be described by an extra Drude term,[36] $g_{\rm D}/\zeta(1 + \tau_{\rm D}\zeta)$, in the Ninham–Parsegian oscillator model. Here $g_{\rm D}$ and $\tau_{\rm D}$ describes the oscillation strength and damping ratio. The gray regime in the inset of Fig. 3 shows the divergence of permittivity induced by the extra Drude term. This divergence drives the Casimir attraction away from

the limit $F(a)/F_0(a) \to$ constant in the micrometer regime.

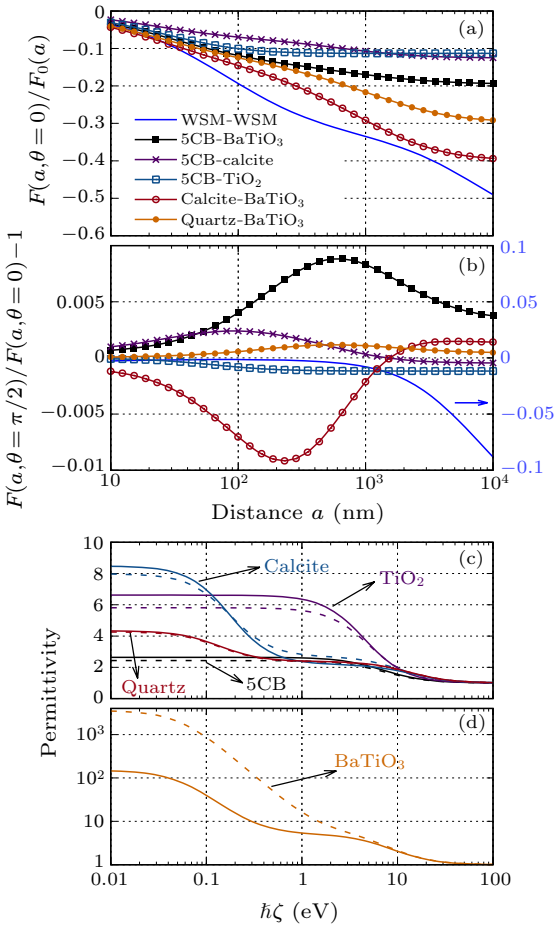

Fig. 4. (a) Casimir force as a function of distance for various uniaxial material systems. The twisting angle $\theta = \theta_2 - \theta_1 = 0$. (b) The maximal relative anisotropy of Casimir force, defined as $F(a,\theta=\pi/2)/F(a,\theta=0)-1$, as a function of distance for the uniaxial material systems given in (a). [(c), (d)] Permittivities of the uniaxial materials. The solid and dashed lines shows the two anisotropic permittivities, $\varepsilon_{\parallel}(i\zeta)$ and $\varepsilon_{\perp}(i\zeta)$, respectively. Detailed parameters can be found from Refs. [37,38].

Another significant influence of chiral anomaly shown in Fig. 2 is the strong anisotropy of Casimir force related to different orientations of the Weyl nodes separations. As a comparison, Fig. 4 shows anisotropic Casimir force in various birefringent materials. The maximal relative anisotropy of Casimir force, defined as $F(a,\theta=\pi/2)/F(a,\theta=0)-1$, is on the magnitude of 1‰ for these conventional birefringent materials. In Fig. 2, for $a = 10\,\mu$m, the maximal ($\boldsymbol{b}_1 = -\boldsymbol{b}_2 \perp xy$ plane) and minimal ($\boldsymbol{b}_1$, $\boldsymbol{b}_2 \parallel xy$ plane, $\theta_2-\theta_1=\pi/2$) Casimir attraction has visible relative anisotropy on the scale of 1/10. The anisotropy of Casimir force is one or even two magnitudes larger than conventional birefringent materials in the micrometer regime, and even more significant when the distance a is larger. The large anisotropy of Casimir force in the micrometer regime provides experimental evidence for the chiral anomaly.

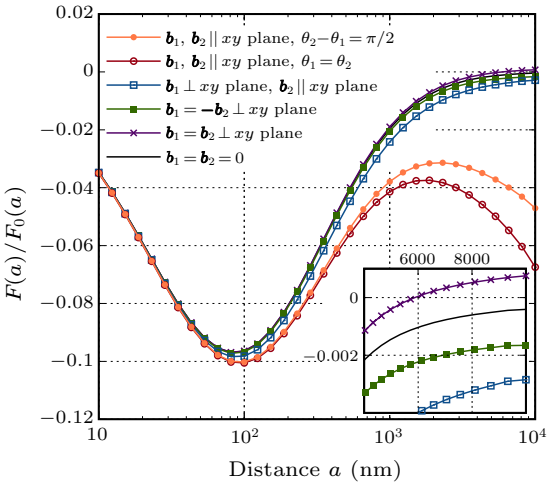

Fig. 5. Casimir force between two WSM slabs (thickness $d = 20$ nm) for different configures of the Weyl node separations. Parameters are chosen to be the same as Fig. 2.

Now we study the Casimir interaction between thin films of WSM. Figure 5 shows Casimir force as a function of distance for $d = 20$ nm and various orientations of $\boldsymbol{b}_1$, $\boldsymbol{b}_2$. Intuitively, one can find that the ratio $F(a)/F_0(a)$ oscillates with the increasing distance between the two WSM slabs, the ratio is enhanced for distance in the range 10–100 nm, reduced for 100–1000 nm, and enhanced again at larger distances for the specific orientations where $\boldsymbol{b}_1$ and $\boldsymbol{b}_2$ are parallel to the interface. The inset shows details of the curves for the distance ranging from 4 μm to 10 μm. Interestingly, one can find that the Casimir force transits from attractive to repulsive at $a \approx 6\,\mu$m for $\boldsymbol{b}_1 = \boldsymbol{b}_2$ perpendicular to the interface. The oscillation of $F(a)/F_0(a)$ in the interval 10–1000 nm is a generic feature of Casimir force between dielectric thin films: when the distance is much greater than the thickness of dielectric films, i.e., $a > 100$ nm in this case, the large-wavelength virtual photon can penetrate into the dielectric films, which makes the Fresnel matrix significantly reduce and the ratio $F(a)/F_0(a)$ decrease correspondingly. For the orientations $\boldsymbol{b}_1$, $\boldsymbol{b}_2$ parallel to the interface, the chiral anomaly induced screening of virtual photon makes the Casimir attraction enhanced as demonstrated for the semi-infinite thickness situation.

The Casimir repulsion that appears in the inset of Fig. 5 is another influence of chiral anomaly if the separation of Weyl nodes is perpendicular to the interface, i.e., $\boldsymbol{b}_1 = \boldsymbol{b}_2 \perp xy$ plane. In this case, the chiral anomaly in WSM can induce a Hall conductivity in the xy plane,[16] $\sigma_{xy} = e^2 b/2\pi^2\hbar$, which modifies the reflection of virtual photon on the surface of WSM by introducing an off-diagonal term. For the normal incidence in the imaginary frequency representation, $k_x = k_y = 0$, the reflection matrices has the following analytic form for the $\boldsymbol{b}_1 = \boldsymbol{b}_2 \perp xy$ plane,

$$\mathbb{R}^{(1)}_{\rm Cart}(i\zeta) = \mathbb{R}^{(2)}_{\rm Cart}(i\zeta) = \begin{pmatrix} r_{xx} & r_{xy} \\ -r_{xy} & r_{yy} \end{pmatrix}, \qquad (12)$$

where

$$r_{yy} = r_{xx},$$
$$r_{xx} = -\frac{(\varepsilon^2-1)\zeta^2+\eta^2}{(\varepsilon-1)^2\zeta^2+\eta^2} + \sum_{\pm}\frac{\lambda_{\pm}\coth(\lambda_{\pm}d)}{(1-\varepsilon)\zeta \pm i\eta}, \quad (13)$$
$$r_{xy} = \frac{2\eta\zeta}{(\varepsilon-1)^2\zeta^2+\eta^2} + \sum_{\pm}\frac{\pm i\lambda_{\pm}\coth(\lambda_{\pm}d)}{(1-\varepsilon)\zeta \pm i\eta}, \quad (14)$$

and $\lambda_{\pm} = \sqrt{\zeta(\varepsilon\zeta \mp i\eta)}$ are the two eigenvalues of the Berreman matrix corresponding to the EM waves with opposite circular polarizabilities. In the thin film limit, $d \to 0$, the reflection matrix is dominated by the terms proportional to $\lambda_{\pm}\coth(\lambda_{\pm}d) \approx 1/d \to \infty$. Furthermore, $r_{xy}/r_{xx} \to \eta/(1-\varepsilon)\zeta \gg 1$ for sufficiently small imaginary frequency ζ. In the large distance limit, $a \to \infty$ and $\zeta \to 0$, one can safely consider only the off-diagonal terms in the reflection matrices. The Lifshitz mode counting function in Eq. (5) simplifies to $\ln(1+e^{-2\kappa a}r_{xy}^2)^2$, this term acquires a minus sign in comparing with the conventional form, and contributes to the repulsive Casimir interaction.[8]

The ratio r_{xy}/r_{xx} is an important index to measure the intensity of Casimir repulsion and attraction, the arc tangent of this ratio defines the Kerr rotation of EM wave reflection on the surface of WSM. For the parameters used in this work, $b = 0.08\,\text{Å}^{-1}$, $d = 20\,\text{nm}$, $\epsilon(0) \approx 13$, and $\zeta = 0.04\text{eV}/\hbar$ for the virtual photon in the micrometer regime, we obtain $\theta_{\text{Kerr}} = \arctan(r_{xy}/r_{xx}) \approx 1$, which estimates that the Casimir repulsion is weak in the micrometer regime.

Until now, the unique experiment, demonstrating that the Casimir–Lifshitz energy stored in the vacuum could be anisotropic, was carried out by Somers *et al.* in the liquid crystal-birefringent material system via measuring the Casimir–Lifshitz torque in the nanometer regime.[6] In this work, we propose another scheme to detect the anisotropic Casimir–Lifshitz energy by measuring the anisotropic Casimir force between WSM slabs for different orientations of $\boldsymbol{b}_1$, $\boldsymbol{b}_2$ in the micrometer regime. The anisotropy of Casimir force is significantly large in comparing with conventional birefringent materials. Furthermore, the chiral anomaly induced screening of virtual photons on the surface of WSM makes the Casimir attraction enhanced in this regime, which makes the measurement more feasible. For WSM thin films, in the micrometer regime, the ratio $F(a)/F_0(a)$ decays to zero rapidly, or even goes into the Casimir repulsive region when the separations of Weyl nodes $\boldsymbol{b}_1 = \boldsymbol{b}_2$ are perpendicular to the interface; the ratio $F(a)/F_0(a)$ can also increase when $\boldsymbol{b}_1$ and $\boldsymbol{b}_2$ are parallel to the interface. This is dramatically different from Casimir interaction in conventional metal, dielectric, and birefringent material. These qualitative differences can be considered as significant evidence of chiral anomaly.

References

[1] Casimir H B G 1948 *Kon. Ned. Akad. Wetensch. Proc.* **51** 793
[2] Munday J N, Capasso F and Adrian P V 2009 *Nature* **457** 170
[3] Sushkov A O, Kim W J, Dalvit D A R and Lamoreaux S K 2011 *Nat. Phys.* **7** 230
[4] Hertlein C, Helden L, Gambassi A, Dietrich S and Bechinger C 2008 *Nature* **451** 172
[5] Wilson C M, Johansson G, Pourkabirian A, Simoen M, Johansson J R, Duty T, Nori F and Delsing P 2011 *Nature* **479** 376
[6] Somers D A T, Garrett J L, Palm K J and Munday J N 2018 *Nature* **564** 386
[7] Levin M, McCauley A P, Rodriguez A W, Reid M T H and Johnson S G 2010 *Phys. Rev. Lett.* **105** 090403
[8] Zhao R, Zhou J, Koschny Th, Economou E N and Soukoulis C M 2009 *Phys. Rev. Lett.* **103** 103602
[9] Zeng R and Yang Y P 2011 *Chin. Phys. Lett.* **28** 054201
[10] Leonhardt U and Philbin T G 2007 *New J. Phys.* **9** 254
[11] Jiang Q D and Wilczek F 2019 *Phys. Rev. B* **99** 125403
[12] Jiang Q D and Wilczek F 2019 *Phys. Rev. B* **99** 165402
[13] Grushin A G and Cortijo A 2011 *Phys. Rev. Lett.* **106** 020403
[14] Tse W K and MacDonald A H 2012 *Phys. Rev. Lett.* **109** 236806
[15] Pablo R L and Grushin A G 2014 *Phys. Rev. Lett.* **112** 056804
[16] Wilson J H, Allocca A A and Galitski V 2015 *Phys. Rev. B* **91** 235115
[17] Wan X G, Turner A M, Vishwanath A and Savrasov S Y 2011 *Phys. Rev. B* **83** 205101
[18] Lv B Q, Xu N, Weng H M, Ma J Z, Richard P, Huang X C, Zhao L X, Chen G F, Matt C E, Bisti F, Strocov V N, Mesot J, Fang Z, Dai X, Qian T, Shi M and Ding H 2015 *Nat. Phys.* **11** 724
[19] Xu S Y, Belopolski I, Alidoust N, Neupane M, Bian G, Zhang C L, Sankar R, Chang G Q, Yuan Z J, Lee C C, Huang S M, Zheng H, Ma J, Sanchez D S, Wang B K, Bansil A, Chou F C, Shibayev P P, Lin H, Jia S and Hasan M Z 2015 *Science* **349** 613
[20] Nielsen H B and Ninomiya M 1981 *Nucl. Phys. B* **193** 173
[21] Nielsen H B and Ninomiya M 1981 *Phys. Lett. B* **105** 219
[22] Nielsen H B and Ninomiya M 1983 *Phys. Lett. B* **130** 389
[23] Adler S L 1969 *Phys. Rev.* **177** 2426
[24] Bell J S and Jackiw R 1969 *Il Nuovo Cimento* **60** 47
[25] Son D T and Spivak B Z 2013 *Phys. Rev. B* **88** 104412
[26] Huang X C, Zhao L X, Long Y J, Wang P P, Chen D, Yang Z H, Liang H, Xue M Q, Weng H M, Fang Z, Dai X and Chen G F 2015 *Phys. Rev. X* **5** 31023
[27] Zyuzin A A and Burkov A A 2012 *Phys. Rev. B* **86** 115133
[28] Grushin A G 2012 *Phys. Rev. D* **86** 045001
[29] Vazifeh M M and Franz M 2013 *Phys. Rev. Lett.* **111** 27201
[30] Goswami P and Tewari S 2013 *Phys. Rev. B* **88** 245107
[31] Zyuzin A A and Zyuzin V A 2015 *Phys. Rev. B* **92** 115310
[32] Hofmann J and Das S S 2016 *Phys. Rev. B* **93** 241402
[33] Berreman D 1972 *J. Opt. Soc. Am.* **62** 502
[34] Dadsetani M and Ebrahimian A 2016 *J. Electron. Mater.* **45** 5867
[35] Milonni P W 1993 *The Quantum Vacuum* (San Diego, Academic Press) pp 230–231
[36] Xu B, Dai Y M, Zhao L X, Wang K, Yang R, Zhang W, Liu J Y, Xiao H, Chen G F, Taylor A J, Yarotski D A, Prasankumar R P and Qiu X G 2016 *Phys. Rev. B* **93** 121110
[37] Munday J N, Iannuzzi D, Barash Y and Capasso F 2005 *Phys. Rev. B* **71** 042102
[38] Somers D A T and Munday J N 2015 *Phys. Rev. B* **91** 032520

Supplementary Materials for "Chiral anomaly enhanced Casimir interaction between Weyl semimetals"

Jia-Nan Rong(荣佳楠)[1,3], Liang Chen(陈亮)[2*], Kai Chang(常凯)[1,3*]

[1] *SKLSM, Institute of Semiconductors, Chinese Academy of Sciences, P. O. Box 912, Beijing 100083, China*
[2] *School of Mathematics and Physics, North China Electric Power University, Beijing, 102206, China*
[3] *CAS Center for Excellence in Topological Quantum Computation, University of Chinese Academy of Sciences, Beijing 100190, China*

Here we show the detailed derivation of the reflection matrices, Eqs. (7) and (8) in the main text, by using the Berreman matrix method. The components of the electric field $\boldsymbol{E}$ and the magnetic field $\boldsymbol{H}$ parallel to the interface, denoted as $\psi(\boldsymbol{k}_\parallel,\omega,z)=(E_x,E_y,H_x,H_y)^{\mathsf{T}}$, have the following solutions in the vacuum,

$$\psi(\boldsymbol{k}_\parallel,\omega,z)=\mathbb{W}e^{\mathbb{K}z}\begin{pmatrix}V_\Downarrow\\V_\Uparrow\end{pmatrix}, \tag{S-1}$$

where

$$\mathbb{W}=\begin{pmatrix}k_3\mathbb{I} & k_3\mathbb{I}\\ \mathbb{Q} & -\mathbb{Q}\end{pmatrix}, \tag{S-2}$$

is consists of the four eigenvectors of the Berreman matrix and $\mathbb{Q}=i\frac{\omega}{c}\begin{pmatrix}-\frac{c^2k_xk_y}{\omega^2} & -1+\frac{c^2k_x^2}{\omega^2}\\ 1-\frac{c^2k_y^2}{\omega^2} & \frac{c^2k_xk_y}{\omega^2}\end{pmatrix}$, $\mathbb{K}=\mathrm{diag}(k_3,k_3,-k_3,-k_3)$ is the matrix consists of the four eigenvalues, $k_3=\sqrt{k_x^2+k_y^2-\omega^2/c^2}$. $\mathbb{I}$ is a 2×2 identity matrix. $(V_\Downarrow,V_\Uparrow)^{\mathsf{T}}$ is a column vector, the subscripts $\Downarrow$ and $\Uparrow$ refer to the propagation directions of EM waves, downward and upward, respectively.

In WSMs, the solution of Maxwell's equations take the same form of Eq. (S1), however, the eigenvector matrix $\mathbb{W}$ and eigenvalue matrix $\mathbb{K}$ take different forms for different situations. Here we consider two different cases, (1) the separation of Weyl nodes in the Brillouin zone, $2b\boldsymbol{e}^{(j)}$, is perpendicular to the interface, i.e., $\boldsymbol{e}^{(1)}=\boldsymbol{e}^{(2)}=\boldsymbol{e}_z$; (2) the separation of the two Weyl nodes is parallel to the interface, i.e., $\boldsymbol{e}^{(j)}=\boldsymbol{e}_x\cos\theta_j+\boldsymbol{e}_y\sin\theta_j$ $(j=1,2)$. For the first case, the Berreman matrix is,

$$\mathbb{B}=i\begin{pmatrix}0 & 0 & \frac{ck_xk_y}{\varepsilon\omega} & \frac{\omega}{c}-\frac{ck_x^2}{\varepsilon\omega}\\ 0 & 0 & -\frac{\omega}{c}+\frac{ck_y^2}{\varepsilon\omega} & -\frac{ck_xk_y}{\varepsilon\omega}\\ i\eta-\frac{ck_xk_y}{\omega} & -\frac{\varepsilon\omega}{c}+\frac{ck_x^2}{\omega} & 0 & 0\\ \frac{\varepsilon\omega}{c}-\frac{ck_y^2}{\omega} & i\eta+\frac{ck_xk_y}{\omega} & 0 & 0\end{pmatrix}. \tag{S-3}$$

The eigen equation, $\mathbb{B}\mathbb{W}=\mathbb{W}\mathbb{K}$, has the following solutions,

$$\mathbb{W}=(W_1,W_2,W_3,W_4), \tag{S-4}$$

$$W_1=\begin{pmatrix}(-\epsilon\frac{\omega^2}{c^2}+k_x^2)p_3\\ (k_xk_y-\sqrt{\varepsilon}\frac{\omega}{c}p_3)p_3\\ -i\sqrt{\varepsilon}(-\varepsilon\frac{\omega^2}{c^2}+k_x^2)\lambda_1\\ -i(\sqrt{\varepsilon}k_xk_y-\varepsilon\frac{\omega}{c}p_3)\lambda_1\end{pmatrix},W_2=\begin{pmatrix}(-\epsilon\frac{\omega^2}{c^2}+k_x^2)p_3\\ (k_xk_y+\sqrt{\varepsilon}\frac{\omega}{c}p_3)p_3\\ i\sqrt{\varepsilon}(-\varepsilon\frac{\omega^2}{c^2}+k_x^2)\lambda_2\\ i(\sqrt{\varepsilon}k_xk_y+\varepsilon\frac{\omega}{c}p_3)\lambda_2\end{pmatrix}, \tag{S-5}$$

$$W_3=\begin{pmatrix}(-\epsilon\frac{\omega^2}{c^2}+k_x^2)p_3\\ (k_xk_y+\sqrt{\varepsilon}\frac{\omega}{c}p_3)p_3\\ i\sqrt{\varepsilon}(-\varepsilon\frac{\omega^2}{c^2}+k_x^2)\lambda_3\\ i(\sqrt{\varepsilon}k_xk_y+\varepsilon\frac{\omega}{c}p_3)\lambda_3\end{pmatrix},W_4=\begin{pmatrix}(-\epsilon\frac{\omega^2}{c^2}+k_x^2)p_3\\ (k_xk_y-\sqrt{\varepsilon}\frac{\omega}{c}p_3)p_3\\ -i\sqrt{\varepsilon}(-\varepsilon\frac{\omega^2}{c^2}+k_x^2)\lambda_4\\ -i(\sqrt{\varepsilon}k_xk_y-\varepsilon\frac{\omega}{c}p_3)\lambda_4\end{pmatrix}, \tag{S-6}$$

where the corresponding eigenvalues $\lambda_1=-\lambda_4=\sqrt{p_3[p_3-i\eta/\sqrt{\varepsilon}]}$, $\lambda_2=-\lambda_3=\sqrt{p_3[p_3+i\eta/\sqrt{\varepsilon}]}$, $p_3=\sqrt{\boldsymbol{k}_\parallel^2-\varepsilon\omega^2/c^2}$, $\varepsilon=\varepsilon(\omega)$ is the dielectric function of WSM. The eigenvalue matrix,

$$\mathbb{K}=\mathrm{diag}(\lambda_1,\lambda_2,\lambda_3,\lambda_4). \tag{S-7}$$

*Corresponding authors. Email: slchern@ncepu.edu.cn; kchang@semi.ac.cn

For the second case, the Berreman matrix is,

$$\mathbb{B}^{(j)}=\begin{pmatrix}\eta\frac{ck_x}{\varepsilon\omega}\sin\theta_j & -\eta\frac{ck_x}{\varepsilon\omega}\sin\theta_j & i\frac{ck_xk_y}{\varepsilon\omega} & i\frac{\omega}{c}-i\frac{ck_x^2}{\epsilon\omega}\\ \eta\frac{ck_y}{\varepsilon\omega}\sin\theta_j & -\eta\frac{ck_y}{\varepsilon\omega}\sin\theta_j & -i\frac{\omega}{c}+i\frac{ck_y^2}{\epsilon\omega} & -i\frac{ck_xk_y}{\varepsilon\omega}\\ -i\frac{ck_xk_y}{\omega}-i\frac{\eta^2c}{\varepsilon\omega}\sin\theta_j\cos\theta_j & -i\frac{\varepsilon\omega}{c}+i\frac{ck_x^2}{\omega}+i\frac{\eta^2c}{\varepsilon\omega}\cos^2\theta_j & \eta\frac{ck_y}{\varepsilon\omega}\cos\theta_j & -\eta\frac{ck_x}{\varepsilon\omega}\cos\theta_j\\ i\frac{\varepsilon\omega}{c}-i\frac{ck_y^2}{\omega}-i\frac{\eta^2c}{\varepsilon\omega}\sin^2\theta_j & i\frac{ck_xk_y}{\omega}+i\frac{\eta^2c}{\varepsilon\omega}\sin\theta_j\cos\theta_j & \eta\frac{ck_y}{\varepsilon\omega}\sin\theta_j & -\eta\frac{ck_x}{\varepsilon\omega}\sin\theta_j\end{pmatrix}. \tag{S-8}$$

The eigen equation, $\mathbb{B}^{(j)}\mathbb{W}^{(j)}=\mathbb{W}^{(j)}\mathbb{K}^{(j)}$, has the following solutions,

$$\mathbb{W}^{(j)}=\left(W_1^{(j)},W_2^{(j)},W_3^{(j)},W_4^{(j)}\right), \tag{S-9}$$

$$W_1^{(j)}=\begin{pmatrix}i[\eta(\eta+\delta^{(j)})+2\varepsilon k_y^2]\frac{\omega}{c}\sin\theta_j+i[\lambda_1^{(j)}(\eta+\delta^{(j)})+2\varepsilon\frac{\omega}{c}k_y\cos\theta_j]k_x\\ -i[\eta(\eta+\delta^{(j)})+2\varepsilon k_x^2]\frac{\omega}{c}\cos\theta_j+i[\lambda_1^{(j)}(\eta+\delta^{(j)})-2\varepsilon\frac{\omega}{c}k_x\sin\theta_j]k_y\\ [\eta(\eta+\delta^{(j)})+2\varepsilon k_x^2]\lambda_1^{(j)}\cos\theta_j+\varepsilon[\frac{\omega}{c}(\eta+\delta^{(j)})+2\lambda_1^{(j)}k_x\sin\theta_j]k_y\\ [\eta(\eta+\delta^{(j)})+2\varepsilon k_y^2]\lambda_1^{(j)}\sin\theta_j-\varepsilon[\frac{\omega}{c}(\eta+\delta^{(j)})-2\lambda_1^{(j)}k_y\cos\theta_j]k_x\end{pmatrix}, \tag{S-10}$$

$$W_2^{(j)}=\begin{pmatrix}i[\eta(\eta-\delta^{(j)})+2\varepsilon k_y^2]\frac{\omega}{c}\sin\theta_j+i[\lambda_2^{(j)}(\eta-\delta^{(j)})+2\varepsilon\frac{\omega}{c}k_y\cos\theta_j]k_x\\ -i[\eta(\eta-\delta^{(j)})+2\varepsilon k_x^2]\frac{\omega}{c}\cos\theta_j+i[\lambda_2^{(j)}(\eta-\delta^{(j)})-2\varepsilon\frac{\omega}{c}k_x\sin\theta_j]k_y\\ [\eta(\eta-\delta^{(j)})+2\varepsilon k_x^2]\lambda_2^{(j)}\cos\theta_j+\varepsilon[\frac{\omega}{c}(\eta-\delta^{(j)})+2\lambda_2^{(j)}k_x\sin\theta_j]k_y\\ [\eta(\eta-\delta^{(j)})+2\varepsilon k_y^2]\lambda_2^{(j)}\sin\theta_j-\varepsilon[\frac{\omega}{c}(\eta-\delta^{(j)})-2\lambda_2^{(j)}k_y\cos\theta_j]k_x\end{pmatrix}, \tag{S-11}$$

$$W_3^{(j)}=\begin{pmatrix}i[\eta(\eta-\delta^{(j)})+2\varepsilon k_y^2]\frac{\omega}{c}\sin\theta_j+i[\lambda_3^{(j)}(\eta-\delta^{(j)})+2\varepsilon\frac{\omega}{c}k_y\cos\theta_j]k_x\\ -i[\eta(\eta-\delta^{(j)})+2\varepsilon k_x^2]\frac{\omega}{c}\cos\theta_j+i[\lambda_3^{(j)}(\eta-\delta^{(j)})-2\varepsilon\frac{\omega}{c}k_x\sin\theta_j]k_y\\ [\eta(\eta-\delta^{(j)})+2\varepsilon k_x^2]\lambda_3^{(j)}\cos\theta_j+\varepsilon[\frac{\omega}{c}(\eta-\delta^{(j)})+2\lambda_3^{(j)}k_x\sin\theta_j]k_y\\ [\eta(\eta-\delta^{(j)})+2\varepsilon k_y^2]\lambda_3^{(j)}\sin\theta_j-\varepsilon[\frac{\omega}{c}(\eta-\delta^{(j)})-2\lambda_3^{(j)}k_y\cos\theta_j]k_x\end{pmatrix}, \tag{S-12}$$

$$W_4^{(j)}=\begin{pmatrix}i[\eta(\eta+\delta^{(j)})+2\varepsilon k_y^2]\frac{\omega}{c}\sin\theta_j+i[\lambda_4^{(j)}(\eta+\delta^{(j)})+2\varepsilon\frac{\omega}{c}k_y\cos\theta_j]k_x\\ -i[\eta(\eta+\delta^{(j)})+2\varepsilon k_x^2]\frac{\omega}{c}\cos\theta_j+i[\lambda_4^{(j)}(\eta+\delta^{(j)})-2\varepsilon\frac{\omega}{c}k_x\sin\theta_j]k_y\\ [\eta(\eta+\delta^{(j)})+2\varepsilon k_x^2]\lambda_4^{(j)}\cos\theta_j+\varepsilon[\frac{\omega}{c}(\eta+\delta^{(j)})+2\lambda_4^{(j)}k_x\sin\theta_j]k_y\\ [\eta(\eta+\delta^{(j)})+2\varepsilon k_y^2]\lambda_4^{(j)}\sin\theta_j-\varepsilon[\frac{\omega}{c}(\eta+\delta^{(j)})-2\lambda_4^{(j)}k_y\cos\theta_j]k_x\end{pmatrix}. \tag{S-13}$$

The corresponding eigenvalues are, $\lambda_1^{(j)}=-\lambda_4^{(j)}=\sqrt{p_3^2+\frac{\eta}{2\varepsilon}(\eta+\delta^{(j)})}$, $\lambda_2^{(j)}=-\lambda_3^{(j)}=\sqrt{p_3^2+\frac{\eta}{2\varepsilon}(\eta-\delta^{(j)})}$, $\delta^{(j)}=\sqrt{\eta^2+4\varepsilon\left(k_x\cos\theta_j+k_y\sin\theta_j\right)^2}$. The eigenvalue matrix for the j-th WSM slab is given by,

$$\mathbb{K}^{(j)}=\mathrm{diag}\left(\lambda_1^{(j)},\lambda_2^{(j)},\lambda_3^{(j)},\lambda_4^{(j)}\right). \tag{S-14}$$

For finite thickness WSMs, there are two boundaries, the wave function ψ is continuous on the boundaries. For the first WSM, these boundary conditions are,

$$\mathbb{W}\begin{pmatrix}0\\E_{\Uparrow}^{[\mathrm{inj}]}\end{pmatrix}+\mathbb{W}\begin{pmatrix}E_{\Downarrow}^{[\mathrm{ref}]}\\0\end{pmatrix}=\mathbb{W}^{(1)}\begin{pmatrix}E_{\Downarrow}^{[\mathrm{WSM}]}\\E_{\Uparrow}^{[\mathrm{WSM}]}\end{pmatrix}, \tag{S-15}$$

$$\mathbb{W}^{(1)}e^{\mathbb{K}^{(1)}d}\begin{pmatrix}E_{\Downarrow}^{[\mathrm{WSM}]}\\E_{\Uparrow}^{[\mathrm{WSM}]}\end{pmatrix}=\mathbb{W}\begin{pmatrix}0\\E_{\Uparrow}^{[\mathrm{tran}]}\end{pmatrix} \tag{S-16}$$

where $E_{\Uparrow}^{[\mathrm{inj}]}$ and $E_{\Downarrow}^{[\mathrm{ref}]}$ denote the injection and the reflection EM wave from the vacuum to the first WSM, $(E_{\Downarrow}^{[\mathrm{WSM}]},E_{\Uparrow}^{[\mathrm{WSM}]})^{\mathsf{T}}$ is the EM wave in the first WSM, $E_{\Uparrow}^{[\mathrm{tran}]}$ is the transmission EM wave. The reflection matrix is defined as,

$$E_{\Downarrow}^{[\mathrm{ref}]}=\mathbb{R}_{\mathrm{Cart}}^{(1)}E_{\Uparrow}^{[\mathrm{inj}]}. \tag{S-17}$$

Solving Eqs. (S15) and (S16), we get Eq. (7) in the main text. Utilizing the same method, we can get Eq. (8).